

# Exploration of all-3d Heusler alloys for permanent magnets: an *ab initio* based high-throughput study

Madhura Marathe\* and Heike C. Herper

*Department of Physics and Astronomy, Uppsala university, 751 20 Uppsala, Sweden.*

(Dated: April 24, 2023)

Heusler alloys have attracted interest in various fields of functional materials since their properties can quite easily be tuned by composition. Here, we have investigated the relatively new class of all-3d Heusler alloys in view of its potential as permanent magnets. To identify suitable candidates, we performed a high-throughput study using an electronic structure database to search for  $X_2YZ$ -type Heusler systems with tetragonal symmetry and high magnetization. For the alloys which passed our selection filters, we have used a combination of density functional theory calculations and spin dynamics modelling to investigate their magnetic properties including the magnetocrystalline anisotropy energy and exchange interactions. The candidates which fulfilled all the search criteria served as input for the investigation of the temperature dependence of the magnetization and determination of Curie temperature. Based on our results, we suggest that  $Fe_2NiZn$ ,  $Fe_2NiTi$  and  $Ni_2CoFe$  are potential candidates for permanent magnets with large out-of-plane magnetic anisotropy (1.23, 0.97 and 0.82 MJ/m<sup>3</sup> respectively) and high Curie temperatures lying more than 200 K above the room temperature. We further show that the magnitude and direction of anisotropy is very sensitive to the strain by calculating the values of anisotropy energy for several tetragonal phases. Thus, application of strain can be used to tune the anisotropy in these compounds.

## I. INTRODUCTION

Discovery of new magnetic materials is vital to improve performance of a range of applications from data storage to renewable energy sources [1]. Permanent magnets constitute an essential component of electric generators used in wind turbines, and large amount of magnetic material is required for each generator [2, 3]. Most commonly used permanent magnets in current devices typically contain rare-earth elements such as neodymium, samarium etc. which make these materials expensive and on top of that their mining is usually harmful to the environment [4]. Therefore, alternative candidates for permanent magnets are highly sought after to improve the overall sustainability. We would like to note that there is an intrinsic limit on the functional response of permanent magnets consisting of light elements determined by associated small spin-orbit coupling [5]. However, we expect such magnets could replace the rare-earth magnets in mid-range applications, and thus reduce the overall dependence on rare earth elements.

What makes a material a good candidate for permanent magnets? – 1. its stability whether it can be synthesized in a given phase and structure: typically preferred symmetries are tetragonal or hexagonal crystal structures so that there is a single well-defined easy axis, 2. large magnetic moments, 3. large magnetocrystalline anisotropy with a preference for out-of-plane magnetization, and 4. Curie temperature above room temperature so that the ferromagnetic state is stable at working conditions for devices. Currently the best strategy to accelerate research into cost-effective and sustainable materials

is to use the high-throughput methods, that is, to comb through a large number of candidates available in various structural databases for alloys and compounds and then to perform electronic structure methods calculations to determine the required physical quantities.

Heusler alloys are intermetallic compounds with  $L2_1$  structure and typically with a chemical formula  $X_2YZ$ . Conventionally X and Y elements are 3d transition metals and Z belongs to either group III, IV or V (main group element). One advantage of these alloys is the easy tuning of its properties obtained by varying the constituent elements, doping, site-disorder and/or strain making these useful for a multitude of functional properties from shape memory effects, half-metallicity to magnetocaloric response; for a general review on Heuslers see the book edited by Felser and Hirohata [6]. Moreover, a number of studies have reported large magnetocrystalline anisotropy in Heusler alloys and have also discussed possibility of its tuning via interstitial doping, strain as well as local ordering of atoms [7–10], thus making Heusler alloys ideal potential candidates for permanent magnets.

In recent years, the conventional Heusler family has expanded to include alloys in which all constituent elements are d-metals [11]. We mainly focus here on magnetic properties of this novel class of Heusler compounds in which Z belongs to 3d metals termed as all-3d Heusler alloys [12–16]. One of the first reports for this type of all-3d Heusler alloy is from Wei *et al.* [12] in which Ni-Mn alloys are doped with Ti to form the Heusler phase and additional Co-doping makes the material a strongly ferromagnetic shape memory alloy. Further studies on their functional responses have reported giant exchange-bias effect [17], giant barocaloric effect [18] as well as large magnetocaloric effect [19, 20]. First-principles calculations have predicted occurrence of martensitic transformation in all-3d  $Zn_2YMn$  ( $Y = Fe, Co$  and  $Ni$ ) alloys [14]

---

\* madhura.marathe@physics.uu.se

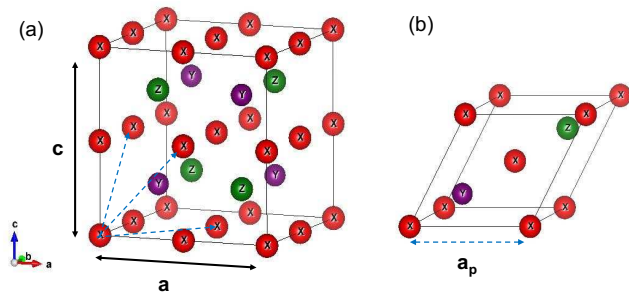


FIG. 1. Unit cell for a typical Heusler alloys of the type  $X_2YZ$  shown for conventional 16-atom (a) and primitive 4-atom (b). Note that the two unit cells are equivalent and blue dashed lines shown in (a) correspond to the primitive cell shown in (b). Here filling of atomic positions corresponds to the “standard” Heusler, whereas the “inverse” structure corresponds to exchange of atoms X and Y occupying positions  $(\frac{1}{2}, \frac{1}{2}, \frac{1}{2})$  and  $(\frac{1}{4}, \frac{1}{4}, \frac{1}{4})$ .

as well as high-spin polarization in  $Fe_2CrZ$  and  $Co_2CrZ$  ( $Z = Sc, Ti$  and  $V$ ) alloys [16].

In this paper, we examine this new class of materials for potential permanent magnets because most of the 3d metals are abundantly found and show strong magnetic interactions, and there exist well-established routes to make alloys in different phases from these metals especially binary alloys of Ni-Fe and Fe-Co and ternary alloys based on these alloys [21]. One of the well-studied transition metal alloys is Fe-Co which has a high saturation magnetization, but small magnetocrystalline anisotropy [21]. This alloy has the body-centered cubic (bcc) structure as the most stable phase, however first-principles calculations have predicted a large anisotropy for Fe-Co in the body-centered tetragonal phase [22, 23]. This observation is confirmed by experiments in which stabilization of the tetragonal phase was achieved by either epitaxial growth [24] or doping with another element [25]. Typically bcc Fe-Co alloys are disordered, however ordered bulk or thin film conventional Heusler alloys of the form  $Fe_2CoZ$  [26, 27] and  $Co_2FeZ$  [28, 29] ( $Z = Si$  or  $Ga$ ) have been synthesized and reported to have large Curie temperatures.

The main objective of our study is the calculation of the relevant magnetic properties such as magnetocrystalline anisotropy and Curie temperatures for a selected set of all-3d Heuslers. It has been shown that strain can be used to tune both the magnitude and the direction of easy-plane axis in Heusler alloys [8, 30]. Thus, we also explore possible tuning of the magnetocrystalline anisotropy for selected alloys via strain engineering. The details of our density functional theory calculations and Monte Carlo simulations are given in Sec. II. The selection of suitable candidates is done using available repository of materials and setting conditions on stability and magnetic moments to filter out materials as described in Sec. III A. The results from our calculations for structural and magnetic properties are presented and discussed in

Sec. III B, then followed by analysis on how we can further tune the properties by strain in Sec. III C. Finally we conclude with a suggestion for a few potential permanent magnets and discuss general outlook for further theoretical and experimental investigations in Sec. IV.

## II. COMPUTATIONAL DETAILS

We perform density functional theory (DFT) calculations using the VASP code [31] to calculate the structural and magnetic properties of Heusler alloys. We use a 16-atom conventional unit cell for these calculations shown in Fig. 1(a). For these calculations, we use the energy cutoff of 650 eV and a k-mesh of  $16 \times 16 \times 16$ . Further we use the generalized-gradient approximation of the Perdew-Burke-Ernzerhof (PBE) type calculated with the projected augmented-wave (PAW) method [32]. To calculate the magnetic anisotropy energy (MAE) and exchange interactions ( $J_{ij}$ ), we make use of the full-potential linearized muffin-tin orbitals (FP-LMTO) code RSPt [33]. To reduce the computational effort, we use a 4-atom primitive unit cell shown in Fig. 1(b) for these calculations. Further a dense k-mesh of  $36 \times 36 \times 36$  is required to accurately capture smaller energy scale for magnetic interactions. The MAE is calculated using the magnetic force theorem [34] and is given by:

$$\mathcal{E}_{MAE} = E_b^{[100]} - E_b^{[001]}, \quad (1)$$

where  $E_b^\alpha$  is the fully-relativistic band energy for the magnetization direction  $\alpha$  calculated from the self-consistent scalar-relativistic potential. Within this definition, a positive  $\mathcal{E}_{MAE}$  corresponds to the uniaxial anisotropy and therefore, indicates a material suitable as a permanent magnet. The exchange parameters are calculated with the Liechtenstein-Katsnelson-Antropov-Gubanov formula [35] as implemented in the RSPt code.

Using the calculated  $J_{ij}$ 's, we map our system on a Heisenberg model given by spin Hamiltonian:

$$\mathcal{H} = - \sum_{ij} J_{ij} \mathbf{e}_i \cdot \mathbf{e}_j, \quad (2)$$

where  $\mathbf{e}_i$  is a unit vector representing local magnetic moment  $m_i$  for site  $i$ . Note that the systems considered in this study contain atoms with partially filled d-electrons and typically have long-range exchange interactions extending over several lattice constants. It is essential that we include these in our model to correctly estimate magnetic properties at finite temperatures. We have included pair-wise  $J_{ij}$ 's for all neighbors  $j$  within  $4.5a$  radius from the central site  $i$  [36]. We perform Monte Carlo (MC) simulations using the UppASD spin dynamics code [37] to obtain finite-temperature properties of the system. Our simulation box has the dimensions  $24 \times 24 \times 24$  and three ensembles are used to reduce the statistical noise in our data. At each temperature, 50,000 steps are used to thermally equilibrate the system and statistical averages of

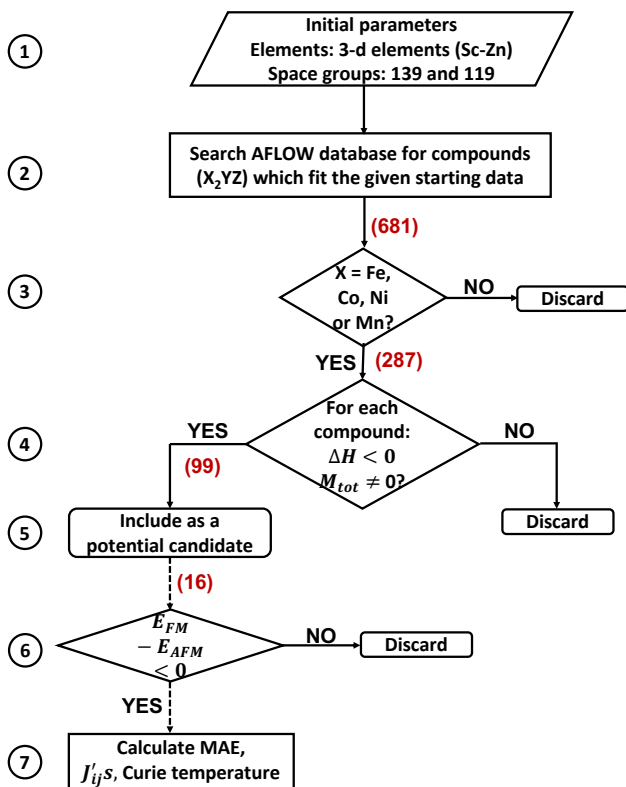


FIG. 2. Flowchart describing a detailed procedure to select the systems for our study (steps 1–5) using the AFLOW database followed by a quick summary of DFT + MC steps for the selected systems (steps 6–7). The number of compounds found after each step is given in brackets. For DFT calculations in step 6, we ensured that there are no duplicate entries and further restricted the pool to those alloys having magnetization larger than 1.0 Tesla. Dashed arrows indicate that only key steps are included here.

physical quantities are taken over next 50,000 steps. A heating cycle is used to calculate the transition temperature with a step size of 20 K in the vicinity of magnetic transition.

### III. RESULTS AND DISCUSSION

#### A. High-throughput systems selection

We used the electronic structure database AFLOW [38, 39] – containing more than 3.5 million material entries – to search for tetragonal Heusler alloys which are stable with negative formation of enthalpy  $\Delta H$  and have magnetization larger than or equal to 1.0 Tesla. We focused on  $X_2YZ$  type of alloys with  $X = \text{Mn, Fe, Co or Ni}$  and both  $Y$  and  $Z$  belong to 3d group from Sc to Zn, that is, we included only 3d transition metals in our search. Both standard and inverse Heusler structures (space group 139 and 119

Compound	$a$ Å	$c/a$	MO	$M_{tot}$ $\mu_B/\text{f.u. Tesla}$	Status
$\text{Mn}_2\text{NiTi}$	5.97	1.48	AFM	0.0 0.0	✗
$\text{Mn}_2\text{TiZn}$	6.01	1.37	FM	4.73 1.01	*
$\text{Fe}_2\text{CoNi}$	5.66	1.33	FM	7.34 1.88	∅
$\text{Fe}_2\text{CoTi}$	5.83	1.65	FM	5.18 1.22	✓
$\text{Fe}_2\text{CoV}$	5.70	1.51	FM	4.21 1.06	✓
$\text{Fe}_2\text{MnTi}$	5.81	1.01	FM	4.16 1.00	∅
$\text{Fe}_2\text{NiSc}$	6.03	1.63	FM	5.06 1.08	∅
$\text{Fe}_2\text{NiTi}$	5.85	1.57	FM	4.50 1.05	✓
$\text{Fe}_2\text{NiZn}$	5.76	1.47	FM	5.59 1.36	✓
$\text{Co}_2\text{FeSc}$	5.97	1.01	FM	4.99 1.09	C
$\text{Co}_2\text{FeTi}^*$	5.81	1.59	FM	4.33 1.03	C
$\text{Co}_2\text{FeZn}$	5.70	1.02	FM	4.91 1.24	C
$\text{Ni}_2\text{CoFe}$	5.61	1.45	FM	5.62 1.49	✓
$\text{Ni}_2\text{FeCu}$	5.65	1.36	FM	3.92 1.01	∅
$\text{Ni}_2\text{MnCu}$	5.69	1.33	AFM	0.0 0.0	✗
$\text{Ni}_2\text{MnZn}$	5.77	1.22	AFM	0.0 0.0	✗

TABLE I. List of all “eligible”  $X_2YZ$  alloys extracted from AFLOW database including their structural parameters obtained from the database. All these compounds except  $\text{Co}_2\text{FeTi}$  (marked with \*) have the standard Heusler phase. The fourth column lists the magnetic ordering and the fifth and sixth columns list the total magnetic moment in different units for each compound calculated using DFT. The last column gives the status of the system with regards to further analysis – ✗: AFM ordering; \*: complex spin ordering; C: cubic structure energetically favored; ∅: small MAE values. All these criteria exclude these alloys from further analysis, whereas ✓ indicates (meta-)stable tetragonal and FM phases with large MAE values suitable for full analysis and are discussed further in the next section.

respectively) are included.<sup>1</sup> A flowchart summarizing our selection procedure is depicted in Fig. 2. In Table I, we have tabulated all the alloys which satisfied our initial filtering criteria described in steps 1–4 and used for DFT calculations in step 6 in Fig. 2. We also list corresponding lattice constant for the cubic phase and  $c/a$  values obtained from the database.

We further analyzed each of the shortlisted structures in the following way. First we performed DFT calculations to check the stability of ferromagnetic (FM) ordering versus antiferromagnetic (AFM) ordering (step 6 in Fig. 2). The corresponding low-energy spin ordering is listed in column four of Table I. For the alloys found to be stable in FM ordering, we have listed the total magnetization  $M_{tot}$  obtained from our calculations in columns

<sup>1</sup> Note that here the exclusion of cubic Heusler alloys (space groups 225 and 216) from our search criteria can be a drawback because even metastable tetragonal phases with negative  $\Delta H$  will be included in our list even when the cubic phase is the most stable phase. However, we examine for such a possibility.

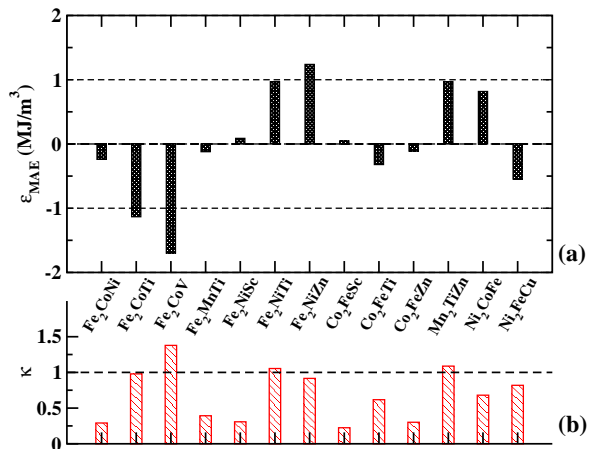


FIG. 3. For all alloys which are found to be ferromagnetic (see Table I) MAE values (a) calculated using Eq. (1) and magnetic hardness parameter  $\kappa$  (b) using Eq. (3) are given.

5 and 6 of Table I. Our values agree well to those reported in the AFLOW database, and all the systems indeed have large magnetic moments. We exclude those alloys for which AFM state is more stable (marked with  $\times$ ) from further analysis.

Most conventional Heusler alloys undergo a structural phase transition between cubic and tetragonal phases depending on constituent elements and applied strain. We have included those alloys which have a negative  $\Delta H$  in the tetragonal phase, but this does not ensure that the most stable phase is indeed tetragonal, and not cubic (see footnote 1). Therefore, for the alloys with the FM ordering, we calculated the structural stability against the tetragonal deformation. We keep the volume constant at the reference structure obtained from the database as we vary  $c/a$  ratio from 0.8 to 1.7 for both standard and inverse phases (discussed in more detail for a few selected alloys later). From this analysis, we confirm that for  $X = \text{Fe}$  and  $\text{Ni}$ , tetragonal phases considered are indeed stable in the T-phase or have a local minima and so could be stabilized by either strain or depositing on a substrate. For  $X = \text{Co}$ , cubic structures are energetically far more favorable which is similar to what is observed for traditional Co-based Heusler alloys [40]. For  $\text{Mn}_2\text{TiZn}$ , the T-phase has a very shallow minima and also shows a tendency towards a more complex ferrimagnetic or AFM ordering with varying  $c/a$  ratio. Therefore, it is not suitable material as a permanent magnet.

In the next step we calculated the magnetocrystalline anisotropy energy for these alloys using Eq. (1). The corresponding results are given in Fig. 3(a). Furthermore using the calculated  $\mathcal{E}_{\text{MAE}}$  and the total magnetic moments, we can estimate the magnetic hardness parameter  $\kappa$  defined as [41]:

$$\kappa = \sqrt{\frac{|\mathcal{E}_{\text{MAE}}|}{\mu_0 M_s^2}}. \quad (3)$$

Here,  $\mu_0 = 4\pi \times 10^{-7} \text{ JA}^{-2}\text{m}^{-1}$  is the vacuum magnetic permeability and  $M_s$  is the saturation magnetization expressed in units of  $\text{Am}^{-1}$ , such that  $\kappa$  is a dimensionless quantity. Typically  $\kappa \gtrsim 1$  is considered as a threshold for hard magnets [41]. The calculated  $\kappa$  values are given in Fig. 3(b). We find that  $\text{Fe}_2\text{NiZn}$ ,  $\text{Fe}_2\text{NiTi}$ ,  $\text{Mn}_2\text{TiZn}$  and  $\text{Ni}_2\text{CoFe}$  alloys have large and positive MAE values indicating a preference to have out-of-plane magnetization. These alloys correspondingly show  $\kappa$  close to 1 with the exceptional case of  $\text{Ni}_2\text{CoFe}$  with  $\kappa \sim 0.7$  which results from its much larger magnetization. Therefore, we would further investigate all these alloys except  $\text{Mn}_2\text{TiZn}$  because of its complex spin ordering. Two alloys  $\text{Fe}_2\text{CoTi}$  and  $\text{Fe}_2\text{CoV}$  also have large but negative MAE which indicates in-plane magnetization is energetically favored as well as  $\kappa$  close to 1. Therefore, these two alloys may also be interesting for applications other than permanent magnets and are included in our subsequent analysis.  $\text{Ni}_2\text{FeCu}$  alloy has a high  $\kappa$  value of 0.8 but rather low  $\mathcal{E}_{\text{MAE}}$  of  $-0.55 \text{ MJ/m}^3$ , and thus is not included as a potential candidate. All the remaining systems have much smaller MAE values of  $\leq |0.5| \text{ MJ/m}^3$  and low  $\kappa$  values therefore are not technologically viable. The last column of Table I summarizes the final status of the each system based on our initial analysis of suitable candidates found in the AFLOW database.

## B. Functional properties of selected alloys

We first discuss in detail our structural analysis for tetragonal phases for the selected five alloys. We performed simulations for a number of tetragonal phases for both standard and inverse structures to determine minimum energy phases. These calculations are done such that the total volume of the unit cell is kept constant at its reference tetragonal structure. In Fig. 4, we have plotted the calculated total energy as a function of  $c/a$  for the selected alloys. We shift the total energy with respect to that of the cubic standard phase of the corresponding alloy for easier comparison.

For  $\text{Fe}_2\text{NiZn}$  and  $\text{Fe}_2\text{NiTi}$  alloys, the standard tetragonal phase is energetically favorable, but this phase is very close in energy to the inverse tetragonal phase as well as to the cubic phase. For  $\text{Fe}_2\text{NiZn}$ , the structure obtained from AFLOW (red star in Fig. 4) is lower in energy by  $1.87 \text{ meV/atom}$  compared to the local minima for the tetragonal inverse at  $c/a = 1.3$  and higher in energy by  $3.99 \text{ meV/atom}$  as compared to the inverse cubic structure, whereas for  $\text{Fe}_2\text{NiTi}$ , the structure from AFLOW is the most stable structure with the corresponding energy differences of  $4.37 \text{ meV/atom}$  with the inverse tetragonal phase at  $c/a = 1.5$  and  $18.4 \text{ meV/atom}$  with the inverse cubic phase; these energy scales are clearly indicated in Fig. 4f. Another interesting feature of the inverse phase energy landscape for both the alloys is that from cubic to compressive strain minimum it is almost flat with very small energy barrier to transform from one phase to an-



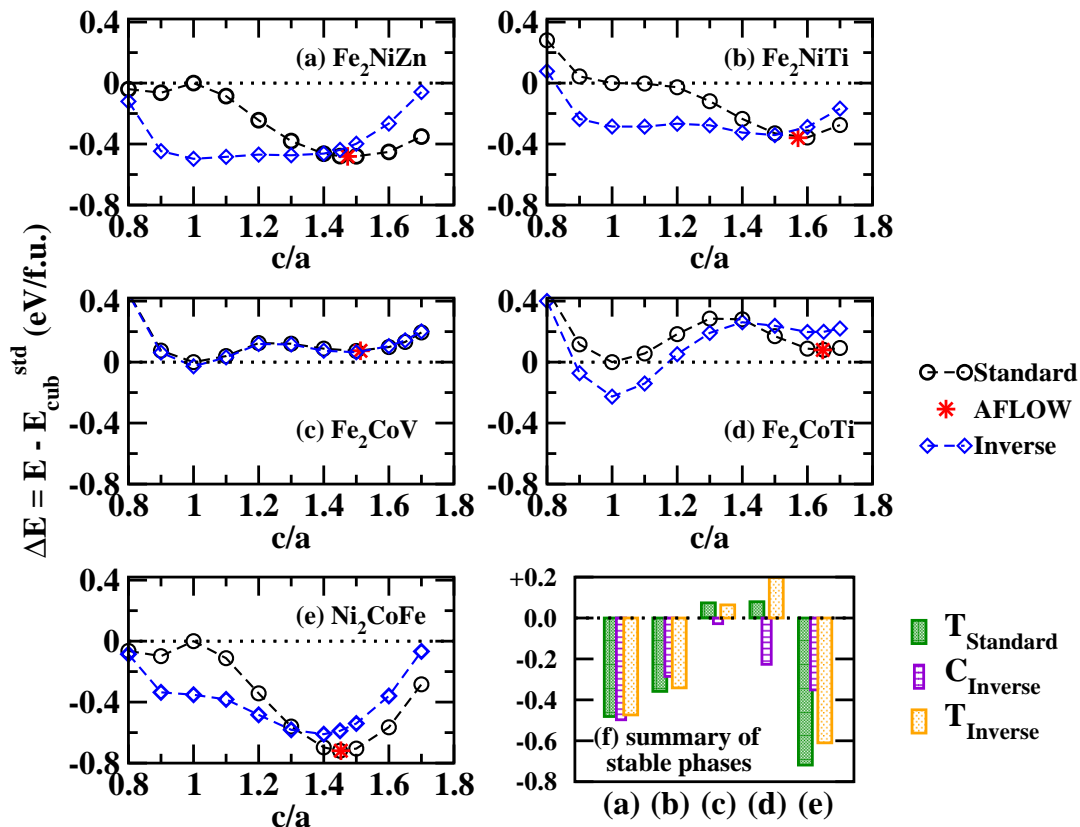


FIG. 4. Stability of tetragonal phases with respect to standard cubic phase: here the energy difference between a distorted structure and the cubic standard phase  $\Delta E$  is plotted as a function of  $c/a$  for  $\text{Fe}_2\text{NiZn}$  (a),  $\text{Fe}_2\text{NiTi}$  (b),  $\text{Fe}_2\text{CoV}$  (c),  $\text{Fe}_2\text{CoTi}$  (d) and  $\text{Ni}_2\text{CoFe}$  (e). The results are shown for both standard and inverse phases along with the structure reported in the AFLOW database. (f) For easier comparison of energy scales, we summarize the  $\Delta E$  values for cubic and the tetragonal phases at the potential well. In all cases, tetragonal standard phase (green bars) corresponds to the AFLOW structure.

other. We have confirmed that the volume of inverse phase does not significantly vary from that of standard phase and small changes in volume do not affect the energy landscape. We note that these are zero temperature calculations, but at room temperature (equivalent to about 25 meV) corresponding free energy landscape may differ. Moreover alloy phases will depend and can be controlled by synthesis conditions.

In contrast to these two alloys where standard and inverse phases show distinct behaviour,  $\text{Fe}_2\text{CoV}$  alloys show almost no dependence on site occupancy by Fe atoms either to form standard or inverse phase as shown in Fig. 4c. This implies a complete site-disorder if this alloy can be formed in the Heusler phase, but it is more likely that it would form body-centered tetragonal phase as was observed in experiments [42]. Also overall the cubic phase is more stable, the tetragonal phase occurs as a local minimum for this alloy. For  $\text{Fe}_2\text{CoTi}$  (Fig. 4d), the standard T-phase is in metastable state compared to the cubic phase and the inverse cubic phase is overall energetically favorable state. Despite their meta-stable structures and in-plane magnetization, we consider both  $\text{Fe}_2\text{CoZ}$  alloys due to their high MAE values and also because it has been shown experimentally that doping

can be used to control the sign of MAE for V-doped Fe-Co alloys [25]. For  $\text{Ni}_2\text{CoFe}$  (see Fig. 4e), the tetragonal phase from AFLOW is indeed the most stable phase observed with the inverse tetragonal phase at  $c/a = 1.4$  lying 27.2 meV/atom higher in energy.

Next, we study finite temperature magnetic properties for the selected five alloys in their tetragonal standard phase corresponding to the AFLOW structure. To map each system on the Heisenberg model, the pair-wise exchange interactions  $J_{ij}$  were computed for all the alloys under study, see Fig. 5. Note that we have calculated the pair-wise interactions between all four sites within the unit cell up to a distance of  $4.5a$  even though we have only shown here only those interactions for which the largest interaction was  $\geq 1$  meV for brevity. As expected, we observe that the nearest-neighbor interactions are the largest in magnitude and positive, i.e. FM coupling. Such strong nearest-neighbor interactions arise from the overlapping 3d orbitals. Often it yields that larger values of  $J_{ij}$  for the nearest neighbor result in a high Curie temperature. However, note that the sign of the interactions changes from positive to negative depending on the distance which implies a competition between FM and AFM coupling within system which may

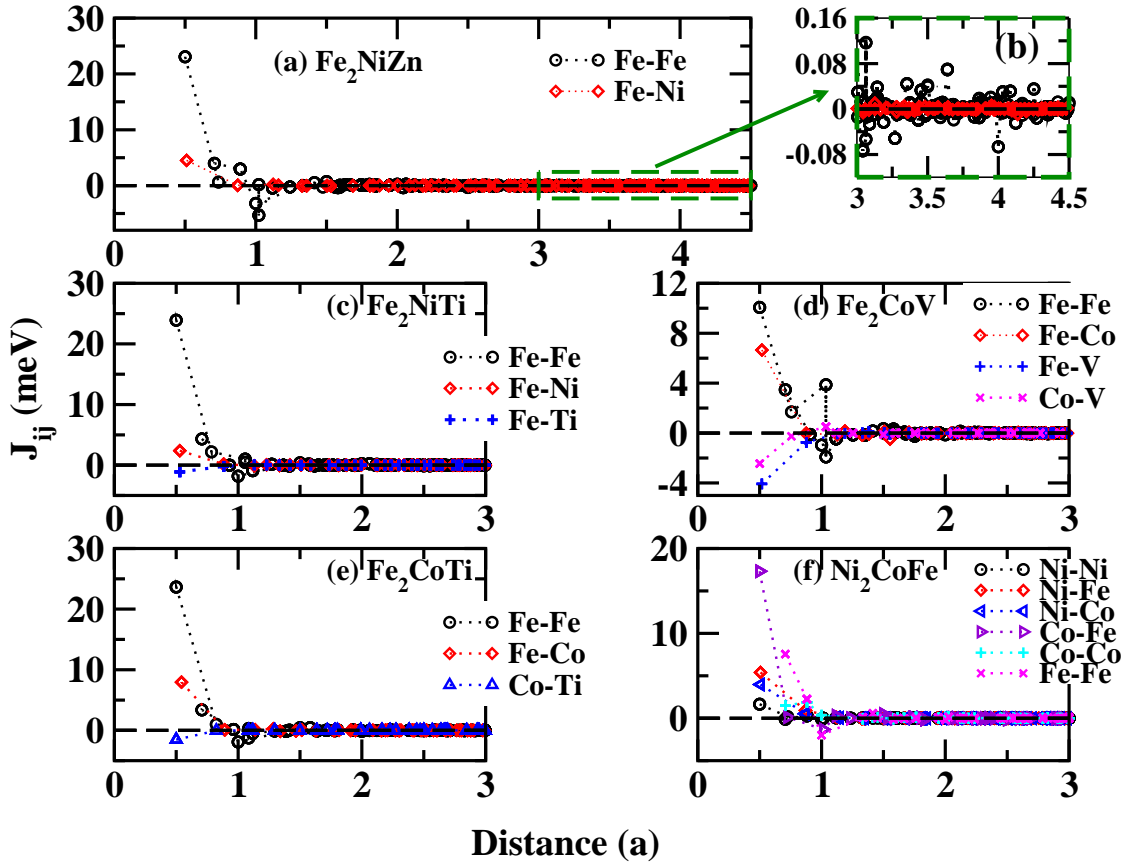


FIG. 5. Calculated pair-wise exchange interactions  $J_{ij}$  for  $\text{Fe}_2\text{NiZn}$  (a),  $\text{Fe}_2\text{NiTi}$  (c),  $\text{Fe}_2\text{CoV}$  (d),  $\text{Fe}_2\text{CoTi}$  (e) and  $\text{Ni}_2\text{CoFe}$  (f): it is plotted as a function of distance between the sites  $i$  and  $j$  given in units of lattice constant of that alloy. A positive  $J_{ij}$  sign corresponds to the ferromagnetic coupling between atoms at  $i$  and  $j$ , whereas a negative sign corresponds to the AFM coupling. Note that the scale is different for y-axis in each panel. In panel (b), we have zoomed in on slowly decaying interactions at larger distances for  $\text{Fe}_2\text{NiZn}$  as an example; for other systems, we have truncated the plots at  $3a$  for clarity.

impact the overall temperature dependence.

For  $Z = \text{Zn}$  and  $\text{Ti}$  alloys, the interactions of  $Z$  with  $X$  and  $Y$  are typically negligible and would not contribute to the magnetic properties of the system. However, for  $Z = \text{V}$  (see Fig. 5d) we observe strong AFM coupling between nearest-neighbor  $\text{Fe-V}$  and  $\text{Co-V}$  of the same order of magnitude as leading FM coupling between  $\text{Fe-Fe}$  and  $\text{Fe-Co}$ . These trends can be understood by looking at the local atomic moments for each alloy tabulated in Table II. Therefore, for a uniform description for all the alloys we retain  $J_{ij}$ 's for all four sites to describe each system. Also note that the  $\text{Ni}_2\text{CoFe}$  alloy differs from other alloy systems because this alloy contains only magnetic 3d metals and therefore results in all FM nearest neighbor interactions, whereas in the remaining alloys there is an AFM coupling between  $Z$  and  $X$  similar to that observed in conventional Heusler alloys.

The magnitude of  $J_{ij}$  decreases as the distance between the sites increases for all  $i$  and  $j$  as is expected. However, the reduction in magnitude is rather slow and even at distances of around  $3a$  (corresponding to about  $15 \text{ \AA}$ ), we observe significant non-zero  $J_{ij}$  values. Use of

Alloy	$M_X$	$M_Y$	$M_Z$
$\text{Fe}_2\text{NiZn}$	2.59	0.56	-0.06
$\text{Fe}_2\text{NiTi}$	2.32	0.36	-0.33
$\text{Fe}_2\text{CoV}$	2.05	1.09	-0.79
$\text{Fe}_2\text{CoTi}$	2.33	1.05	-0.35
$\text{Ni}_2\text{CoFe}$	0.69	1.69	2.76

TABLE II. Local moments on different atomic sites for the selected  $X_2YZ$  alloys are tabulated in  $\mu_B$ . Note that the two sites occupied by atoms  $X$  for these alloys are equivalent and have the same moment. Similar to the conventional Heusler alloys the first four alloys  $Z$  atom ( $\text{Ti}$ ,  $\text{V}$  or  $\text{Zn}$ ) has induced moment with opposite sign which is also reflected in  $J_{ij}$ 's shown in Fig. 5.

a dense k-mesh ensures that we do not see any noise. As an example, in panel (b) we have zoomed in on the tail part of  $J_{ij}$ 's for  $\text{Fe}_2\text{NiZn}$  between  $3-4.5a$ . Note that the values are of the order of  $0.1 \text{ meV}$  and vary between FM and AFM coupling. It has been reported that these oscillating long-range interactions originate from Ruderman-Kittel-Kasuya-Yoshida interactions mediated via conduc-

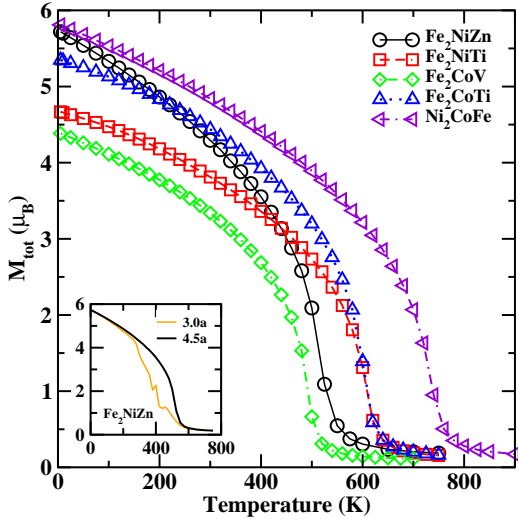


FIG. 6. Curie temperature calculation: total magnetic moment as a function of temperature obtained from Monte Carlo simulations is plotted for different alloys. The inset compares the corresponding data for  $\text{Fe}_2\text{NiZn}$  calculated by including only short-range  $J_{ij}$  interactions within the model.

tion electrons [43]. Similar behaviour is observed for all the system considered here (not shown) and exclusion of these large distance interactions can impact simulations of finite temperature properties as discussed later. Similar long tails for exchange interactions have been reported for conventional Heusler alloys as well [36].

To obtain the finite temperature properties of the alloys we fed the  $J_{ij}$ 's to the Heisenberg model given in Eq. (2). The resulting total magnetic moments of the system  $M_{tot}$  as a function of temperature are plotted in Fig. 6. As expected  $M_{tot}$  decreases slowly as temperature increases due to random orientations of magnetic moment of each individual atom at different sites arising from thermal fluctuations. As a result, the material undergoes a second-order phase transition to a paramagnetic phase at high temperatures. Note that for the alloys under study magnetic transition occurs at much higher temperature than the room temperature. The calculated Curie temperature  $T_c$  which corresponds to the peak in susceptibility from magnetization curves (not shown here) is highest for  $\text{Ni}_2\text{CoFe}$  at 740 K followed by  $\text{Fe}_2\text{NiTi}$  (620 K) and  $\text{Fe}_2\text{CoTi}$  (600 K) and then  $\text{Fe}_2\text{NiZn}$  (520 K) and  $\text{Fe}_2\text{CoV}$  (500 K).

Based solely on the largest observed FM interaction, we would expect that the largest  $T_c$  for  $\text{Fe}_2\text{NiTi}$ ,  $\text{Fe}_2\text{NiZn}$  or  $\text{Fe}_2\text{CoTi}$ . However, this strong FM coupling is counterbalanced by AFM coupling among next nearest neighbors and the largest  $T_c$  is observed  $\text{Ni}_2\text{CoFe}$  for which all leading coupling terms are FM because of presence of all magnetic metals and AFM coupling is much smaller. The strongest effect of such competition is observed for  $\text{Fe}_2\text{CoV}$  in which strong AFM coupling of vanadium with Fe and Co (Fig. 5d) reduces both Curie temperature and total magnetization at zero temperature.

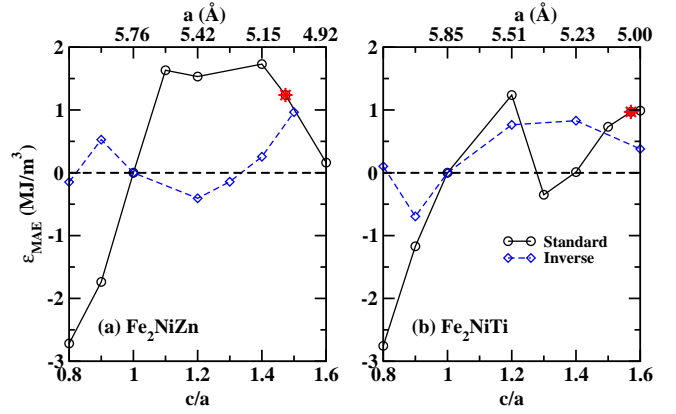


FIG. 7. Effect of tetragonality on magnetic anisotropy: we have plotted here the calculated MAE for  $\text{Fe}_2\text{NiZn}$  (a) and  $\text{Fe}_2\text{NiTi}$  (b) as a function of  $c/a$  ratio for both standard and inverse phases, and the corresponding in-plane lattice constants  $a$  are indicated at the top of the plot. The AFLOW structure is highlighted with a red star and the corresponding MAE values are those shown in Fig. 3.

These results correspond to the inclusion of  $J_{ij}$ 's corresponding to all the neighboring sites within the distance of  $4.5a$ . To establish the effect of long-range interactions on temperature-dependence, we have compared the temperature-dependence of  $M_{tot}$  for  $\text{Fe}_2\text{NiZn}$  when we exclude  $J_{ij}$ 's for sites at a distance larger than  $3a$  as shown in the inset of Fig. 6. Note that near the transition temperature there is a lot of statistical noise in the data and the system does not undergo a smooth transition. Such noise typically implies that the system has competing phases and is not able to reach equilibrium. For MC simulations, this may arise from either inadequate sampling or because “model material” does not describe the “real” system completely. Additional tests showed that the noise is not reduced by increasing either the system size, simulation time or the number of ensembles to improve the quality of the data. However, including long-range interactions results in a smoother transition confirming that the long-range nature of exchange interactions is essential in the Heisenberg model for these systems. This noise can be explained by competing FM and AFM coupling present at larger distance shown in Fig 5(b). Therefore, we conclude that for materials containing 3d-transition metals it is important to check convergence of long-distance interactions for better predictive power of simulations.

### C. Tuning of MAE

As discussed at the beginning of Sec. III B, the alloys studied here show two minima (either global or local) at the cubic phase and the tetragonal phase with certain compressive strain. These two structural phases and the standard and inverse phases arising from chemical

site ordering are shown to have small energy differences, therefore it should be possible to achieve these phases by applying strain or using different substrates for growing thin films. Typically for 3d elements, the d-orbitals lying near the Fermi level contribute the most to MAE [44], and shape and position of d-orbitals is quite sensitive to structure, strain and chemical environment for the metal, which in turn means that MAE too is sensitive to these changes. Therefore, next we examine the effect of tetragonality and site-occupancy on the MAE values for the most promising alloys:  $\text{Fe}_2\text{NiZn}$  and  $\text{Fe}_2\text{NiTi}$ . Note that even though  $\text{Ni}_2\text{CoFe}$  has the highest  $T_c$  and is quite stable in its tetragonal phase compared to the cubic phase, its constituent elements tend to form binary alloys with several competing phases [21] making synthesis of  $\text{Ni}_2\text{CoFe}$  in Heusler structure very difficult. These arguments based on existing binary phase diagrams are further confirmed by calculation of the phonon dispersion for these three alloys to check for dynamic stability of each phase; see Supplemental Material appended at the end for details. This alloy system therefore would require more detailed study based on free energy analysis and is not considered for strain tuning.

The calculated MAE values as a function of  $c/a$  are plotted in Fig. 7 for both standard and inverse phases. In agreement with earlier observations, we observe that the strain leads to changes in the magnitude of MAE and also results in rotation of the easy plane axis from out-of-plane to in-plane axis for both standard and inverse phases. For inverse phases (blue diamonds), overall smaller  $|\mathcal{E}_{\text{MAE}}|$  is observed for both strain regimes. Significantly for applications, in the vicinity of stable AFLOW structures (shown with red star) values of MAE are comparable for standard and inverse phases. This indicates that site disorder should not affect the MAE for these alloys.

For both alloys in the standard phase, the MAE is negative for tensile strains implying in-plane magnetization, its magnitude increases with increasing strain. However, we observe highly non-monotonic trends in MAE as we go from tensile ( $c/a < 1$ ) to compressive ( $c/a > 1$ ) strain. For  $\text{Fe}_2\text{NiZn}$  standard phase, the tetragonal phases with  $c/a$  between 1.1 to 1.5 have large positive MAE of  $> 1 \text{ MJ/m}^3$  which is very promising for applications, whereas for  $\text{Fe}_2\text{NiTi}$ , positive MAE observed for the ground state ( $c/a = 1.57$ ) reduces almost to zero at  $c/a = 1.4$  before going to a large positive value of  $1.2 \text{ MJ/m}^3$  at  $c/a = 1.2$ . This trend implies that very accurate control of growth or preparation condition would be needed for potential applications for the latter alloy. For conventional Ni-based Heusler alloys, the density of states analysis based on occupation and position of d-orbitals worked well [8], however for the alloys studied here the correlation is more complex and not obvious. Based on the in-plane lattice constants for cubic and tetragonal phases (indicated as top x-axis in Fig. 7), we suggest a few suitable substrates – GaAs having lattice constant  $4.00 \text{ \AA}$  for cubic phases or Cu with  $3.61 \text{ \AA}$  for tetragonal phases at the local minima (see Table 1 in

Ref. [45]) – which have small lattice mismatch calculated with respect to  $a_p = a/\sqrt{2}$  and therefore can be used to grow the “correct” phase for tuning anisotropy.

#### IV. SUMMARY AND CONCLUSIONS

We used a combination of high-throughput database search, density functional theory calculations and Monte Carlo simulations to study a new subclass of Heusler alloys – all-3d Heuslers – as potential candidates for permanent magnets. After application of first filters with a set of criteria we obtained about 20 systems with tetragonal symmetry and high magnetic moments in the AFLOW database. For these alloys, we performed a thorough examination of preferred easy-plane axis and Curie temperatures to find three potential candidates –  $\text{Fe}_2\text{NiZn}$ ,  $\text{Fe}_2\text{NiTi}$  and  $\text{Ni}_2\text{CoFe}$  – with magnetocrystalline anisotropy of the order of  $1 \text{ MJ/m}^3$  with preferred out-of-plane magnetization and which remain ferromagnetic for at least 200 K above the room temperature. For  $\text{Fe}_2\text{NiZn}$  and  $\text{Fe}_2\text{NiTi}$ , the energy landscape is rather flat implying strain can stabilize the tetragonal phase. We further showed for these alloys that strain engineering is a viable option to further tune their anisotropy and site disorder between Fe and Ni would not reduce MAE significantly. A few conventional Heusler alloys show potential for spintronics applications, however, we obtain low spin polarization values for these alloys (see Supplemental Material appended at the end). Therefore, these three alloys do not appear viable for spintronics applications.

We also found two alloys –  $\text{Fe}_2\text{CoV}$  and  $\text{Fe}_2\text{CoTi}$  – with high Curie temperature and large MAE, but with in-plane easy axis. These alloys are good candidates for further studies to examine whether alloying and/or doping can be used to rotate the easy axis. Moreover some of the alloys which did not pass our initial filters for permanent magnets showed some promising properties and could be studied further for applications such as magnetocalorics.

Our study opens up a new class of rare-earth free permanent magnets with extensive potential possible via thin film growth for strain tuning. We would like to note that due to absence of heavy metals, there is admittedly a limit to the largest anisotropy obtained within this class of Heusler alloys. However, there exists a large market for intermediate applications of permanent magnets which do not require strong anisotropy. We believe that usage of these magnets for such applications can result in overall reduction in dependence on the rare-earth metals.

#### V. ACKNOWLEDGEMENTS

We acknowledge financial support from Olle Engkvist foundation, StandUp, eSENCE, the Swedish Strategic



Research Foundation (SSF) (Grant EM16-0039), and the ERC. Computational resources and support was provided by the Swedish National Infrastructure for Computing (SNIC) at NSC (Linköping) and PDC (KTH Stockholm).

MM also thanks Patrik Thunström and Rafael Vieira for fruitful discussions and technical support running the RSPT and UppASD codes.

- 
- [1] O. Gutfleisch, M. A. Willard, E. Brück, C. H. Chen, S. G. Sankar, and J. P. Liu, *Advanced Materials* **23**, 821 (2011).
- [2] M. J. Kramer, R. W. McCallum, I. A. Anderson, and S. Constantinides, *JOM* **64**, 752 (2012).
- [3] L. H. Lewis and F. Jiménez-Villacorta, *Metallurgical and Materials Transactions A* **44**, 2 (2013).
- [4] G. Bailey, N. Mancheri, and K. Van Acker, *Journal of Sustainable Metallurgy* **3**, 611 (2017).
- [5] J. H. van Vleck, *Phys. Rev.* **52**, 1178 (1937).
- [6] C. Felser and A. Hirohata, eds., *Heusler alloys: Properties, Growth, Applications*, Springer series in Material Science No. 222 (Springer, 2016).
- [7] Y.-I. Matsushita, G. Madjarova, J. K. Dewhurst, S. Shallcross, C. Felser, S. Sharma, and E. K. U. Gross, *Journal of Physics D: Applied Physics* **50**, 095002 (2017).
- [8] H. C. Herper, *Phys. Rev. B* **98**, 014411 (2018).
- [9] Q. Gao, I. Opahle, O. Gutfleisch, and H. Zhang, *Acta Materialia* **186**, 355 (2020).
- [10] V. V. Sokolovskiy, O. N. Miroshkina, V. D. Buchelnikov, and M. E. Gruner, *Phys. Rev. Mater.* **6**, 025402 (2022).
- [11] V. G. de Paula and M. S. Reis, *Chemistry of Materials* **33**, 5483 (2021).
- [12] Z. Y. Wei, E. K. Liu, J. H. Chen, Y. Li, G. D. Liu, H. Z. Luo, X. K. Xi, H. W. Zhang, W. H. Wang, and G. H. Wu, *Applied Physics Letters* **107**, 022406 (2015).
- [13] Z. Y. Wei, E. K. Liu, Y. Li, X. L. Han, Z. W. Du, H. Z. Luo, G. D. Liu, X. K. Xi, H. W. Zhang, W. H. Wang, and G. H. Wu, *Applied Physics Letters* **109**, 071904 (2016), <https://doi.org/10.1063/1.4961382>.
- [14] Z. Ni, Y. Ma, X. Liu, H. Luo, H. Liu, and F. Meng, *Journal of Magnetism and Magnetic Materials* **451**, 721 (2018).
- [15] Z. Ni, X. Guo, X. Liu, Y. Jiao, F. Meng, and H. Luo, *Journal of Alloys and Compounds* **775**, 427 (2019).
- [16] K. Özdoğan, I. V. Maznichenko, S. Ostanin, E. Şaşıoğlu, A. Ernst, I. Mertig, and I. Galanakis, *Journal of Physics D: Applied Physics* **52**, 205003 (2019).
- [17] S. Samanta, S. Ghosh, and K. Mandal, *Journal of Physics: Condensed Matter* **34**, 105801 (2021).
- [18] A. Aznar, A. Gràcia-Condal, A. Planes, P. Lloveras, M. Barrio, J.-L. Tamarit, W. Xiong, D. Cong, C. Popescu, and L. Mañosa, *Phys. Rev. Materials* **3**, 044406 (2019).
- [19] S. Samanta, S. Ghosh, S. Chatterjee, and K. Mandal, *Journal of Alloys and Compounds* **910**, 164929 (2022).
- [20] S. Samanta, S. Chatterjee, S. Ghosh, and K. Mandal, *Phys. Rev. Materials* **6**, 094411 (2022).
- [21] E. P. Wohlfarth, ed., *Ferromagnetic materials: A handbook on the properties of Magnetically ordered substances*, Vol. 2 (North-Holland Publishing company, 1980) Chap. 2.
- [22] T. Burkert, L. Nordström, O. Eriksson, and O. Heinonen, *Phys. Rev. Lett.* **93**, 027203 (2004).
- [23] K. Hyodo, Y. Kota, and A. Sakuma, *Journal of the Magnetics Society of Japan* **39**, 37 (2015).
- [24] F. Yildiz, M. Przybylski, X.-D. Ma, and J. Kirschner, *Phys. Rev. B* **80**, 064415 (2009).
- [25] T. Hasegawa, T. Niibori, Y. Takemasa, and M. Oikawa, *Scientific Reports* **9**, 5248 (2019).
- [26] Y. Du, G. Z. Xu, X. M. Zhang, Z. Y. Liu, S. Y. Yu, E. K. Liu, W. H. Wang, and G. H. Wu, *EPL (Europhysics Letters)* **103**, 37011 (2013).
- [27] A. K. Jana, M. M. Raja, J. A. Chelvane, P. Ghosal, and S. N. Jammalamadaka, *Journal of Magnetism and Magnetic Materials* **521**, 167528 (2021).
- [28] S. Wurmehl, G. H. Fecher, H. C. Kandpal, V. Ksenofontov, C. Felser, H.-J. Lin, and J. Morais, *Phys. Rev. B* **72**, 184434 (2005).
- [29] P. J. Brown, K. U. Neumann, P. J. Webster, and K. R. A. Ziebeck, *Journal of Physics: Condensed Matter* **12**, 1827 (2000).
- [30] H. C. Herper and A. Grünebohm, *IEEE Transactions on Magnetics* **55**, 1 (2019).
- [31] G. Kresse and J. Furthmüller, *Computational Materials Science* **6**, 15 (1996).
- [32] G. Kresse and D. Joubert, *Phys. Rev. B* **59**, 1758 (1999).
- [33] J. M. Wills, M. Alouani, P. Andersson, A. Delin, O. Eriksson, and O. Grechnev, *Introduction to electronic structure theory, in Full-Potential Electronic Structure Method: Energy and Force Calculations with Density Functional and Dynamical Mean Field Theory* (Springer Berlin Heidelberg, Berlin, Heidelberg, 2010) pp. 25–34.
- [34] X. Wang, D. sheng Wang, R. Wu, and A. Freeman, *Journal of Magnetism and Magnetic Materials* **159**, 337 (1996).
- [35] A. Liechtenstein, M. Katsnelson, V. Antropov, and V. Gubanov, *Journal of Magnetism and Magnetic Materials* **67**, 65 (1987).
- [36] P. Entel, A. Dannenberg, M. Siewert, H. C. Herper, M. E. Gruner, D. Comtesse, H.-J. Elmers, and M. Kallmayer, *Metallurgical and Materials Transactions A* **43**, 2891 (2012).
- [37] O. Eriksson, A. Bergman, L. Bergqvist, and J. Hellsvik, *Ab-initio spin-dynamics: foundations and applications* (Oxford University Press, 2017).
- [38] <https://afLOW.org/>.
- [39] F. Rose, C. Toher, E. Gossett, C. Oses, M. B. Nardelli, M. Fornari, and S. Curtarolo, *Computational Materials Science* **137**, 362 (2017).
- [40] S. Trudel, O. Gaier, J. Hamrle, and B. Hillebrands, *Journal of Physics D: Applied Physics* **43**, 193001 (2010).
- [41] J. M. D. Coey, *IEEE Transactions on Magnetics* **47**, 4671 (2011).
- [42] K. Takahashi, M. Sakamoto, K. Kumagai, T. Hasegawa, and S. Ishio, *Journal of Physics D: Applied Physics* **51**, 065005 (2018).
- [43] E. Şaşıoğlu, L. M. Sandratskii, and P. Bruno, *Phys. Rev. B* **77**, 064417 (2008).
- [44] H. Takayama, K.-P. Bohnen, and P. Fulde, *Phys. Rev. B* **14**, 2287 (1976).
- [45] L. Zhu and J. Zhao, *Applied Physics A* **111**, 379 (2013).
- [46] A. Togo and I. Tanaka, *Scripta Materialia* **108**, 1 (2015).

**SUPPLEMENTARY DATA FOR “EXPLORATION  
OF ALL-3D HEUSLER ALLOYS FOR  
PERMANENT MAGNETS: AN *AB INITIO*  
BASED HIGH-THROUGHPUT STUDY”**

For  $\text{Fe}_2\text{NiZn}$ ,  $\text{Fe}_2\text{NiTi}$  and  $\text{Ni}_2\text{CoFe}$  – three alloys which show promising magnetic properties – we have done additional analysis. The following results are obtained for the stable tetragonal phase found from density functional theory calculations shown in Fig. 4 of the manuscript.

### S1. PHONON BAND STRUCTURES

We used PHONOPY [46] code to obtain phonon dispersion curves for the tetragonal phases of three Heusler alloys. The calculations were performed within the harmonic approximation using the finite displacement method. We used a  $2 \times 2 \times 2$  supercell constructed from a conventional 16-atom unit cell and used displacement of  $0.01\text{\AA}$  to calculate the forces with the VASP code [31]. Other computational details are the same those used to perform structural analysis.

The calculated phonon frequencies along the high-symmetry paths in the Brillouin zone are plotted in Fig. 8. We indeed find that both  $\text{Fe}_2\text{NiZn}$  and  $\text{Fe}_2\text{NiTi}$  alloys are dynamically stable with no imaginary frequencies observed in the phonon dispersion, whereas we get unstable phonon modes at the  $\Gamma$  point for  $\text{Ni}_2\text{CoFe}$ . Unstable  $\Gamma$  modes typically indicate that atoms prefer to displace with respect to each other. This is expected in the case of  $\text{Ni}_2\text{CoFe}$  because its constituent elements have very stable binary phases and the Heusler tetragonal phase studied here is likely to be unstable. These results confirm our arguments based on binary phase diagrams of Fe-Co and Fe-Ni, that this system would not be a suitable candidate as a permanent magnet. On the other hand, the dynamic

stability of  $\text{Fe}_2\text{NiZn}$  and  $\text{Fe}_2\text{NiTi}$  corroborates that these two alloys are ideal permanent magnet candidates. Here, we would like to note that we have not relaxed the structure of the systems to allow for shape changes, so there is a possibility that the system prefers symmetry other than tetragonal as the ground state. However, a full analysis of all symmetries is beyond the scope of this paper.

### S2. DENSITY OF STATES

For  $\text{Fe}_2\text{NiZn}$ ,  $\text{Fe}_2\text{NiTi}$  and  $\text{Ni}_2\text{CoFe}$ , we also examined the spin polarized density of states shown in Fig. 9. This was calculated for the conventional 16-atom unit cell using the VASP package. For  $\text{Fe}_2\text{NiZn}$  and  $\text{Ni}_2\text{CoFe}$ , the majority spin channel is almost completely occupied, whereas for  $\text{Fe}_2\text{NiTi}$  there is a small pseudo-gap at the Fermi level  $E_f$ . This typically can result in large spin polarization values defined by:

$$\sigma = \frac{\rho_{\uparrow} - \rho_{\downarrow}}{\rho_{\uparrow} + \rho_{\downarrow}}, \quad (4)$$

where  $\rho_{\uparrow}$  and  $\rho_{\downarrow}$  correspond to the density of states at Fermi level for spin up and down electrons respectively. The calculated  $\sigma$  values for  $\text{Fe}_2\text{NiZn}$ ,  $\text{Fe}_2\text{NiTi}$  and  $\text{Ni}_2\text{CoFe}$  are about 69%, 56.6% and 40.7% respectively. These low values result from the existence of sharp peaks of localized d-states in the minority channel. Because of the existence of multiple localized d-states near  $E_f$ , small changes in the structure, strain may result in shifting of peaks such that the Fermi energy lies not at the maximum, but at a minimum, and will result in spin polarization which is sensitive to external parameters. For applications, materials are required to have robust values which can be sustained over a large operational range. Based on these results, we conclude that these Heusler alloys are not half-metallic in nature and therefore would not be suitable for spintronics applications.

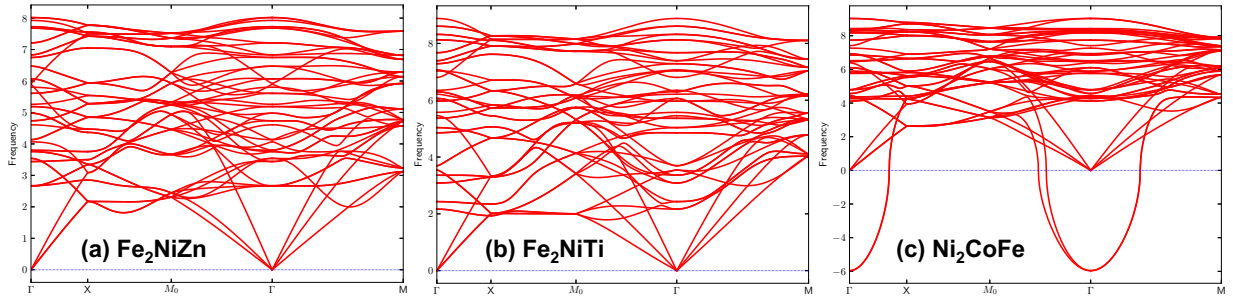


FIG. 8. Calculated phonon band dispersion for the tetragonal Heusler alloys  $\text{Fe}_2\text{NiZn}$  (a),  $\text{Fe}_2\text{NiTi}$  (b) and  $\text{Ni}_2\text{CoFe}$  (c).

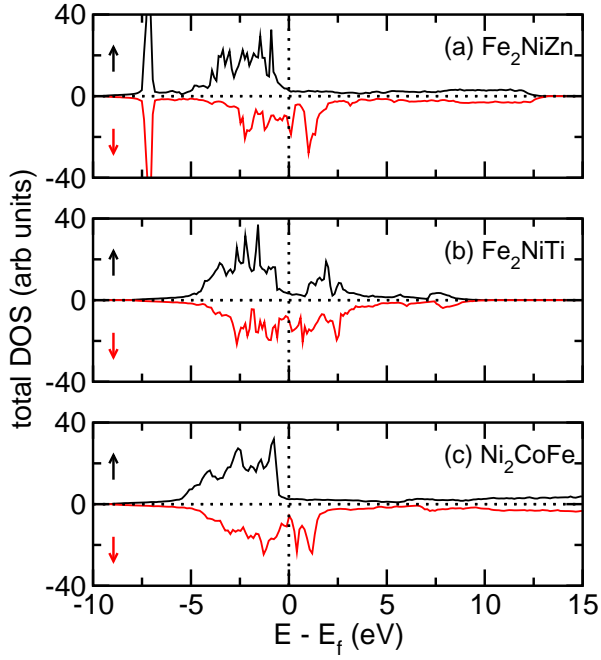


FIG. 9. Spin polarized density of states calculated for the tetragonal Heusler alloys  $\text{Fe}_2\text{NiZn}$  (a),  $\text{Fe}_2\text{NiTi}$  (b) and  $\text{Ni}_2\text{CoFe}$  (c).